

# Thermo-Mechanical Stresses and Mechanical Reliability of Multilayer Ceramic Capacitors (MLCC)

Jin-Woo Park<sup>†</sup>

Department of Metallurgical System Engineering, College of Engineering, Yonsei University, Seoul, Korea

Jeong-Hoon Chae,\* Il-Hyun Park, and Hyuk-Joon Youn

Passive Components Team (MLCC R&D Group), Samsung Electro-Mechanics, Suwon, Korea

Yang-Ho Moon

Fundamental Technology Center (CAE Group), Corporate R&D Institute, Samsung Electro-Mechanics, Suwon, Korea

**In this work, the effects of design parameters on the mechanical reliability of multilayer ceramic capacitors (MLCC) are evaluated by a board flex test. Using the finite element method (FEM), thermo-mechanical stresses that accumulated in the ceramic of MLCC during termination firing, soldering, and board flex test are determined by varying design parameters. The calculation results revealed that the sizes of Cu terminations are the parameters that affect the stress the most. The degree of sensitivity of the stress to the dominant parameters depends significantly on the thickness ratio of the MLCC to the board. Based on our investigation, better design rules are proposed and verified experimentally.**

## I. Introduction

THERE has been an increasing need for multilayer ceramic capacitors (MLCC) in various applications due to their high capacitance per volume and excellent high-frequency characteristics.<sup>1,2</sup> The wide applications of MLCC include surface-mounted circuits (SMC) in telecommunications, automotive engineering, and aeronautics.<sup>1,3</sup> With various applications, the assembling processes and operating conditions of SMC have become diverse, which has increased the concern about the reliability of MLCC.<sup>4</sup>

MLCCs are exposed to more than ten reliability tests including thermal shock, board flex (bending), and biased humidity tests, etc., depending on the targeted applications.<sup>5</sup> Among the reliability tests, the board flex test evaluates the mechanical resistance to cracking when MLCCs are subjected to bending stress on the printed circuit board (PCB) that the MLCC is soldered on.<sup>3</sup> The bending of PCB can occur frequently during handling between manufacturing steps and during operations under temperature variations.<sup>6</sup> The cracking by the bending stresses causes low DC resistance, short circuit, or significant loss of capacitance that can result in critical failure of a complete circuit.<sup>6</sup> According to the reliability standard,<sup>5</sup> a change in the capacitance of MLCC should be less than  $\pm 12.5\%$  under 2~3 mm board bending (depending on the applications).

The cross section of the board flex test specimen and the typical fracture pattern of MLCC are described schematically in Fig. 1. Cracks are usually initiated in the ceramic at the end of the Cu termination.<sup>7,8</sup> Owing to different thermo-mechanical

properties of the ceramic and Cu termination, thermal residual stresses are accumulated in the MLCC on cooling from the termination firing temperatures.<sup>2,3</sup> During the soldering process, an additional thermal stress is superimposed. Higher stress levels are superimposed in those parts of the MLCC that are closer to the board. Conclusively, the largest tensile residual stress is induced in the ceramic along the bottom interface edges E<sub>1</sub>–E<sub>4</sub> in Fig. 1.<sup>8</sup> When bending load is applied, fracture occurs in the ceramic at a much lower stress than the bending stress of the monolithic ceramic as the residual tensile stress is higher.<sup>9</sup>

Engineers have addressed this problem by modifying the design parameters.<sup>3,7,8</sup> The effect of the parameters has been investigated using the finite element method (FEM). However, the FEM analysis was two-dimensional; hence, some calculation results seem to yield conclusions contradictory to experimental observations.<sup>3</sup> The parameters that were studied previously have been limited to soldering process parameters and a few design parameters that are related to the capacitance of MLCC.<sup>3,8</sup> The former is under the user's control and the latter cannot be modified easily even if we know better designs. The cracking of MLCC in the board flex test is influenced by many parameters simultaneously. Without an in-depth understanding of the factors determining the stress in the MLCC, direct comparison between the calculation and experimental results is difficult.

In this study, the mechanism of stress development in MLCC is investigated using a three-dimensional FEM simulation. Using the standard composite theory,<sup>10</sup> the thick laminated active layer is reduced or a part of the active layers is simplified into

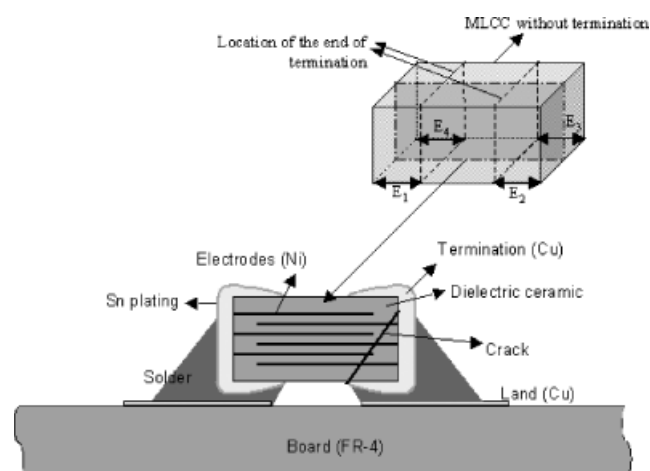


**Fig. 1.** Schematic descriptions of the cross section of the board flex test specimen and the typical crack shape.

G. Rodel—contributing editor

Manuscript No. 22549, Received December 5, 2006; approved March 6, 2007.

\*Current address: Samyoung Electronics, Sung-Nam, Korea.

<sup>†</sup>Author to whom correspondence should be addressed. e-mail: jwpark@alum.mit.edu

**Table I. Descriptions of Two MLCC Models**

	Type of MLCC	Chip size <sup>†</sup>	Chip thickness (Chip T, mm)**	Number of layers in active layers	Thickness of the dielectric layer (μm)**	Thickness of Ni electrode (μm)**
Model A	X7R	2012	0.85	13	35	1.7
Model B		2012	1.25	63	15	1.7

<sup>†</sup>First two digits indicate the length of MLCC and the last two digits represent the width in increments of 0.1 mm. \*\*The size of the each part is measured after binder dry-out process.

an equivalent homogeneous anisotropic solid.<sup>10–12</sup> Hence, the three-dimensional FEM calculations can be carried out with reasonable time efficiency and without sacrificing numerical accuracy.

Using the maximum principal stress ( $\sigma_{p,max}$ ) in the ceramic as a failure metric, the effects of various design parameters on the stress are investigated. Based on our theoretical understandings and calculation results, the parameters affecting on the stress the most are determined and design rules are proposed. The design rules are verified experimentally.

## II. Numerical Analysis and Experimental Procedures

### (1) Numerical Calculation and Model Descriptions

Two MLCC models analyzed in this study are described in Table I. Three-dimensional FEM models of a 1/4 MLCC and a 1/4 board flex test specimen of Model A in Table I are shown in Figs. 2(a) and (b), respectively. MLCC consists of thick laminate active layers comprising a large number of repeating layers of a ceramic and an electrode sandwiched between two covers and

two margins. The material of each part is also described in Figs. 2(a) and (b). Based on the observations under optical microscopy (OM) and scanning electron microscopy (SEM), the FEM model, particularly, the shapes of the solder and the Cu termination are made as similar as possible to the real specimen. Solder only wets the land and the Cu termination. Thin Sn plating layers in Fig. 1 are not included in the FEM models.

The configurations of the active layers are modified using the standard composite theory<sup>10</sup> for constructing optimized FEM models. Because the Ni electrode is thin compared with other parts of the test specimen and the total number of layers is large, it is difficult to construct an FEM model of the test specimen that allows calculations to be performed within a reasonable time without sacrificing numerical accuracy. The configuration of the modified active layers and effective material properties in Models A and B will be explained in detail in Section II(2) and Appendix A.

The continuum analysis simulates cooling from the termination firing temperature (850°C) to room temperature ( $T_R$ ). The static analysis also includes subsequent heating ( $T_R$  to 250°C) and cooling (250°C to  $T_R$ ) of the soldering process and the three-point bending (3 mm) of the board flex test as described in Fig. 3. Uniform cooling is assumed and time-independent, temperature-dependent material properties are used.<sup>3,14</sup> For the termination, the Ni electrodes, the land, and the solder, elastic-plastic material responses are modeled (Table II).<sup>3</sup> Anisotropic thermo-elastic properties are used for the FR-4 board.<sup>14</sup>

In the sensitivity analysis, the effect of parameters in Table III on the stress distribution of  $\sigma_{p,max}$  and corresponding peak value in the ceramic is investigated. Parameters related to the configuration of the active layers are not modified. Stress is calculated by varying one parameter in the range given in Table III, while the other parameters are fixed. The ranges of parameters in Table III were determined based on the size requirements for each MLCC model.

The sizes of each parameter in Table III are the values measured after the binder dry-out process. After termination firing, MLCC is densified; hence, the sizes of the design parameters are changed. However, predicting the degree of densification is beyond the scope of this study. Among the parameters in Table III,  $t_b$  (the maximum thickness of the termination on the upper and bottom sides of MLCC) and  $t_s$  (the maximum thickness of the termination on the side of MLCC) (Fig. 2(a)) cannot be controlled separately with current production capability. Hence,  $t_b - t_s$  is treated as a single parameter in this study. The FEM calculation results are obtained using the ABAQUS computer program.<sup>15</sup> Calculation results are summarized into analytical formulations using a regression method (DOE-PRO<sup>16</sup>).

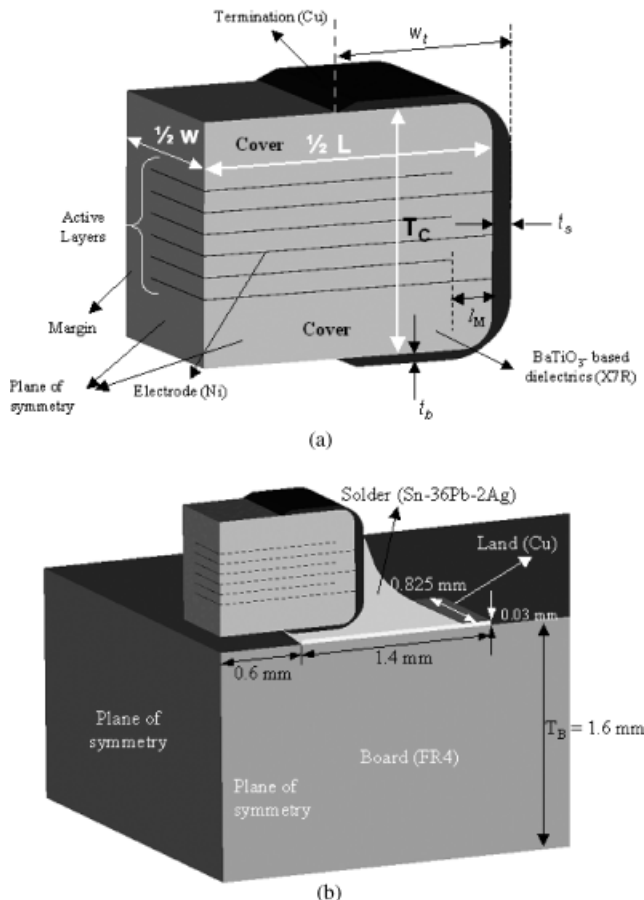


**Fig. 2.** Finite element method (FEM) models of (a) 1/4 multilayer ceramic capacitors (MLCC) Model A, (b) 1/4 board flex test specimen of Model A.

**Table II. Material Properties (At Room Temperature)<sup>13</sup>**

	CTE ( $10^{-6}/^{\circ}\text{C}$ )	Young's modulus (GPa)	Poisson ratio	Yield stress (MPa)
Ceramic	7.60	175	0.25	—
Ni (electrode)	13.3	208	0.33	148
Cu (termination, land)	16.7	128	0.33	75.8
Sn-36Pb-2Ag	24.7	26.5	0.36	36.4

Table III. Design Parameters and the Ranges Varied for the Sensitivity Analysis

Thickness of the termination ( $t_b$ - $t_s$ , $\mu\text{m}$ )	Termination Width ( $w_t$ , $\mu\text{m}$ )	Cover thickness ( $\mu\text{m}$ )	Margin length ( $\mu\text{m}$ )	Solder height to chip T (%)	
MLCC A	13-35 ~ 30-70	400 ~ 590	100 ~ 200	130 ~ 240	20 ~ 100
MLCC B	20-50 ~ 50-100	450 ~ 660			

### (2) Laminate Composite Model for Active Layers

One-eighth of the active layers is schematically described in Fig. A-1 in Appendix A. Although Part B of the active layers in Fig. A-1 has a different volumetric ratio of the electrode to the dielectric ceramic ( $V_e/V_d$ ) from Part A, the whole active layers are simplified into one laminate composite because  $l_M/L$  ( $=0.12$ ) is small. Based on the standard composite theory,<sup>10</sup> the laminate composites can be represented by an equivalent homogeneous anisotropic solid<sup>11,12</sup> or replaced by a composite with a smaller number of layers. In other words, if  $V_e/V_d$  is fixed, the active layers will have the same thermo-mechanical responses under loading, regardless of the number of layers,  $n$ .<sup>11,12</sup> Depending on the loading conditions, there is a certain limitation in the minimum value of  $n$ .<sup>11</sup>

In Model A, the number of layers is decreased in half to double the thickness of each layer. Model B has almost five times larger number of layers than Model A. Except for several layers adjacent to each cover, the rest of the active layers are replaced by a homogenized anisotropic solid with effective properties in Model B. The effective properties are calculated in terms of volumetric ratio,  $f_i (= \frac{V_i}{V_{\text{Total}}}, i = d, e)$ , and thermo-elastic properties of each layer using the classical composite theory,<sup>10</sup> which are described in Appendix A. The several layers close to the covers are made two times thicker than the real thickness of the electrode in Table III, with  $V_e/V_d$  fixed.

### (3) Board Flex Test

The configuration of the board flex test is described in Fig. 3. Solder paste is screen printed on two lands and the MLCCs are surface mounted manually on the paste. After reflow soldering, 20 samples of Models A and B without any abnormal cracks in the exterior appearance are board flex tested (Fig. 3(a), Texture Analyzer, QTS-25, CNS Farnell Corp., London, UK). As shown in Fig. 3(a), bending is applied up to the maximum flex

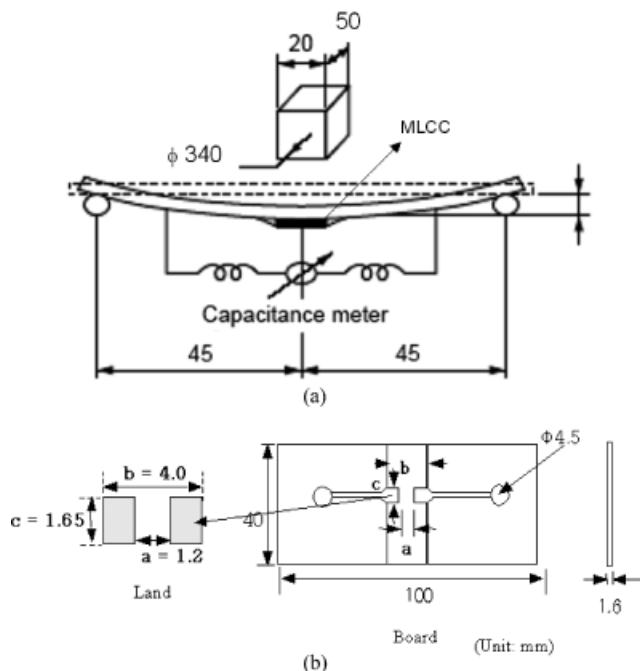


Fig. 3. Schematic description of the configurations of (a) the board flex test and (b) the test board.

point, 3 mm, at a speed of 0.3 mm/s and the change in capacitance is measured. The board is kept bent at the maximum flex point for 5 s. If the change in capacitance is less than  $\pm 12.5\%$  of the expected value,<sup>5,6</sup> the bending continue to be increased up to 10 mm by 0.5 mm.

A test specimen yielding a change in capacitance larger than  $\pm 12.5\%$  is polished carefully, and the surface is observed with an optical microscope. The same procedure is repeated until the central cross section is observed. By examining multiple cross sections from the surface to the center, the three-dimensional crack path can be investigated. Selected cross sections are molded for SEM.

## III. Results

### (1) Numerical Results

According to the calculation results, a large tensile stress is induced in the ceramic on the interfaces with the Cu termination

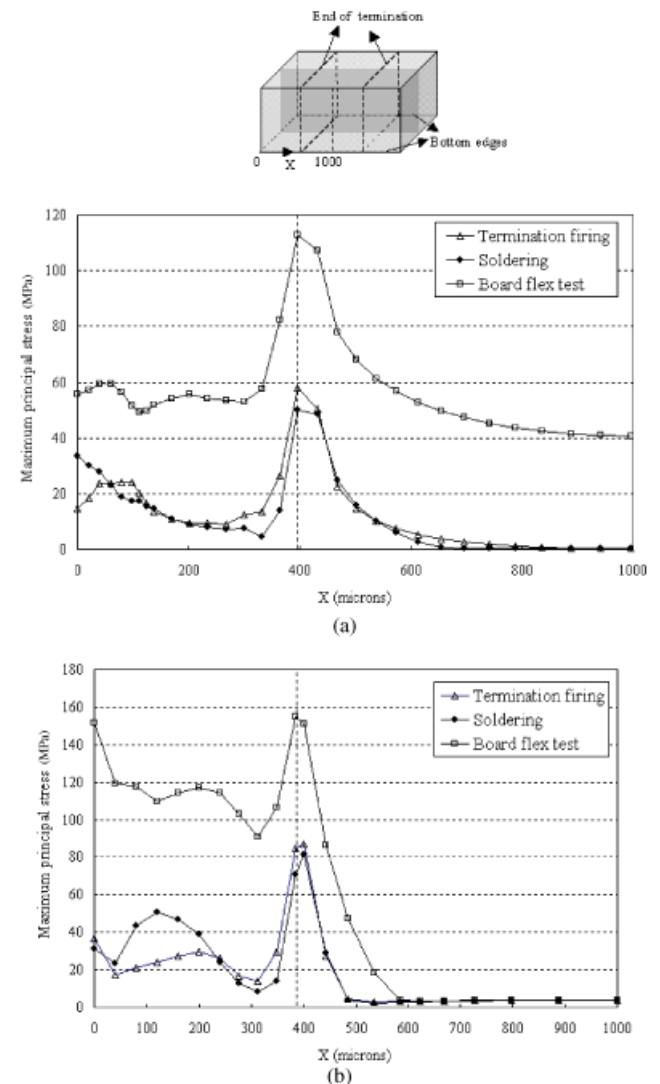


Fig. 4. Maximum principal stress along the bottom edge of (a) Model A and (b) Model B.

and adjacent to the end of the Ni electrode below the covers when cooling down from the termination firing temperature. In the soldering and the board flex test, there are negligible changes in magnitude and distribution of the stress adjacent to the Ni electrode. However, on the bottom cover/termination interfaces, the tensile stress becomes larger. As a result, the accumulated stress in the three processes is the largest along the bottom interface edges depicted in Fig. 4.

In Figs. 4(a) and (b), the maximum principal stresses ( $\sigma_{p,max}$ ) along the bottom edges at the end of the three processes are compared. The MLCCs used in Figs. 4(a) and (b) are Model A with termination of  $w_t = 450 \mu\text{m}$ ,  $t_b = 13 \mu\text{m}$ , and  $t_s = 35 \mu\text{m}$ , and Model B with termination of  $w_t = 450 \mu\text{m}$ ,  $t_b = 20 \mu\text{m}$ , and  $t_s = 50 \mu\text{m}$ , respectively. As shown in Figs. 4(a) and (b), peak stress occurs at the end of termination on cooling from the termination firing temperature. The changes in the magnitude and distribution of  $\sigma_{p,max}$  by soldering are negligible. However, the board flex test increases  $\sigma_{p,max}$  significantly.

In the test specimen of Model A, the board bending of 3 mm increases  $\sigma_{p,max}$  by 40–50 MPa uniformly along the bottom edge as shown in Fig. 4(a). However, in the specimen of Model B,  $\sigma_{p,max}$  is increased only along the interface with the termination. Different effects of bending on the stress development in Models A and B are shown more clearly in Fig. 5. As shown in Fig. 5(a), bending superimposes tensile stress in almost the bottom half of the MLCC in Model A. A strong tensile stress concentration is obtained at the end of termination on the bottom

interface edge. In contrast to Model B, tensile stress is induced only on a small volume close to the bottom and front interfaces with the termination by bending, but a high stress concentration is obtained on a larger bottom interface area than in Model A.

According to the sensitivity analysis,  $w_t$  and  $t_b - t_s$  are the most important parameters affecting  $\sigma_{p,max}$  in both Models A and B. The solder height also affects  $\sigma_{p,max}$ , but its effect is secondary. The effect of changing margin size is negligible. Within the range in Table III, the cover size is also a secondary parameter. However, increasing cover size over a certain value in Model A makes its thickness ratio of the MLCC to the board ( $T_C/T_B$ ) close to that of Model B, which will affect the magnitude and distribution of stress significantly. As already shown in Figs. 4 and 5, the effect of bending load on the stress development is quite different in Models A and B, which results primarily from the different  $T_C/T_B$  of the two models.

Figures 6(a) and (b) show the changes of  $\sigma_{p,max}$  along the bottom cover/termination interfaces of Models A and B in the board flex test by varying  $w_t$  with fixed  $t_b - t_s$  (20–50  $\mu\text{m}$ ) for Model A and 35–75  $\mu\text{m}$  for Model B). In Model A, the greatest  $\sigma_{p,max}$  always occurs at the end of termination and its magnitude is affected significantly by  $w_t$ . According to the calculation results, increasing  $w_t$  decreases the greatest  $\sigma_{p,max}$  in termination firing process in Model A. However, the degree of reduction in the greatest  $\sigma_{p,max}$  becomes less as  $w_t$  is increased over a certain value. As mentioned previously, changes in the stress by soldering are negligible, but almost the same magnitude of stress is

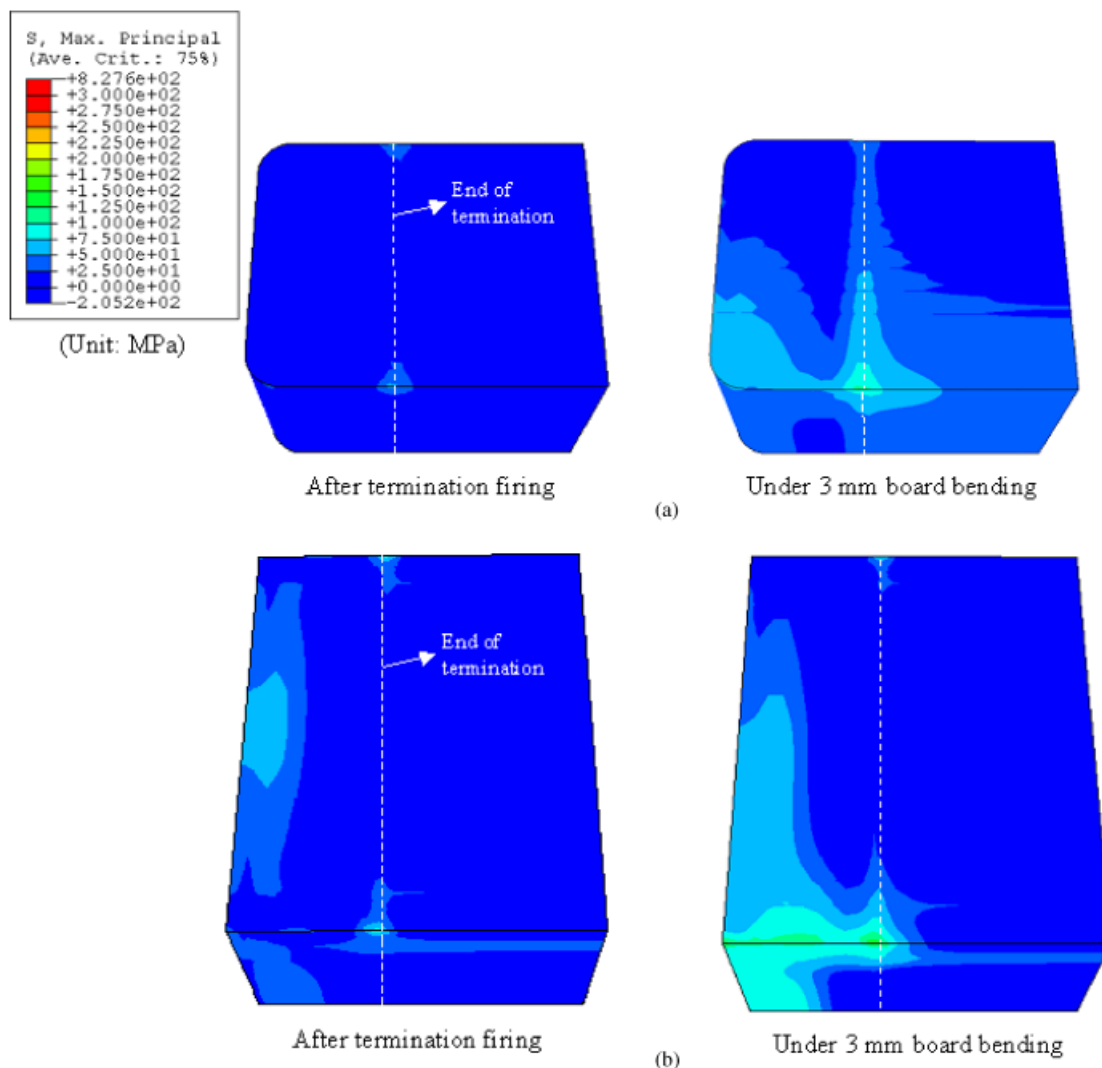


**Fig. 5.** Comparison of  $\sigma_{p,max}$  contours after termination with under 3 mm board bending in 1/4 multilayer ceramic capacitors (MLCC) without the termination of (a) Model A and (b) Model B.

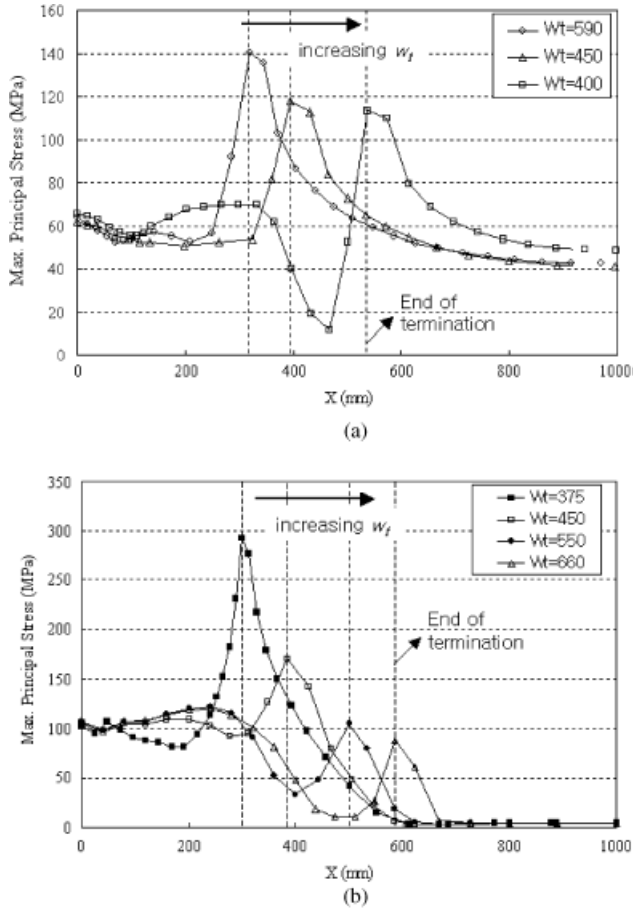


**Fig. 6.** Maximum principal stress ( $\sigma_{p, \max}$ ) along the bottom edge (X direction in Fig. 4) in 3 mm bending in (a) Model A and (b) Model B with different  $w_t$ .

superimposed uniformly on the bottom edges in Model A when bending the board. Hence, the differences in  $\sigma_{p, \max}$  along the bottom edges resulting from different  $w_t$  remain almost the same from the termination firing process to the board flex test.

In Model B, the effect of increasing  $w_t$  on the stress induced in termination firing process shows the same tendency as Model A based on the FEM results. In addition, the same magnitude of increase in  $w_t$  results in a greater reduction in the greatest  $\sigma_{p, \max}$  than in Model A. However, in the board flex test, a larger  $w_t$  is not always good for reducing stress in Model B. As already shown in Fig. 5(b), stress increased along the interface with termination by bending is not constant. According to the calculation results, the magnitude of the overlay is the smallest at the end of termination and increases toward the end of the interface edge. Hence, as shown in Fig. 6(b), the location of the greatest  $\sigma_{p, \max}$  is not always at the end of termination depending on  $w_t$ . As  $w_t$  increases, the peak stress is decreased; however, stress increases along the interface. On increasing  $w_t$  over a certain value ( $> \sim 550 \mu\text{m}$ ), the location of the greatest  $\sigma_{p, \max}$  is shifted from the end of termination to the interface close to the corner of MLCC as shown in Fig. 6(b). The greatest  $\sigma_{p, \max}$  on the interface is not affected by the further increase in  $w_t$ .

Varying  $t_b - t_s$  and  $w_t$  simultaneously within the ranges in Table III, the changes in the greatest  $\sigma_{p, \max}$  in the board flex test are summarized in Figs. 7(a) and (b). In Model A, the greatest  $\sigma_{p, \max}$  becomes smaller as  $t_b - t_s$  is smaller and  $w_t$  is larger as shown in Fig. 7(a). Within the given boundaries, the optimum values for  $w_t$  and  $t_b - t_s$  to minimize  $\sigma_{p, \max}$  are  $w_t = 590$ ,  $t_b - t_s = 13\text{--}35 \mu\text{m}$ . In Model B, as  $t_b - t_s$  is increased, the effect of increasing  $w_t$  on reducing the greatest  $\sigma_{p, \max}$  is enhanced. The filled squares and circles in Fig. 7(b) indicate that  $\sigma_{p, \max}$  occurs on the interface, not at the end of termination. As shown in Fig. 7(b), stress increase on the interface exceeds the peak stress

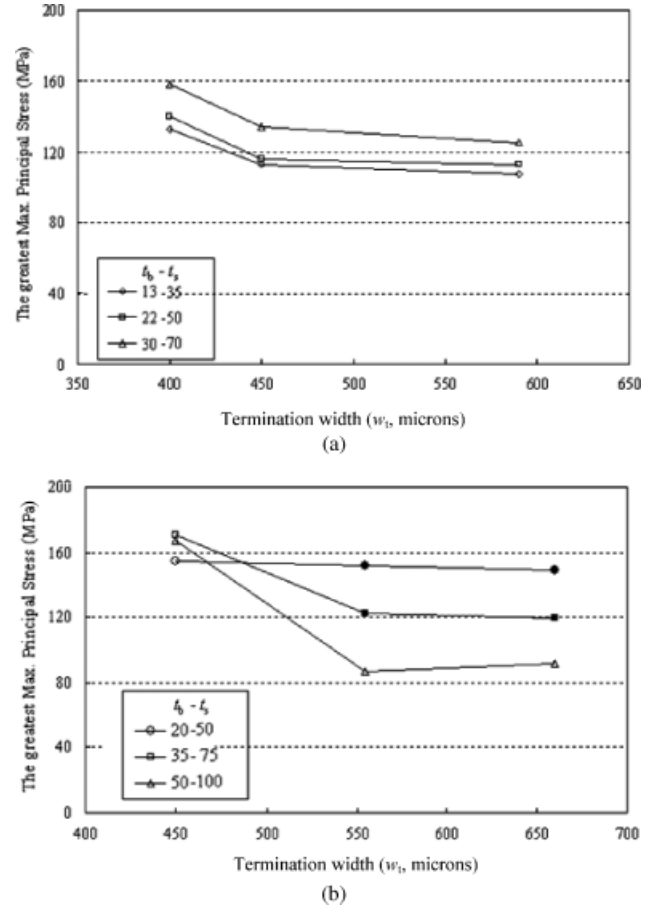


**Fig. 7.** Changes in the greatest maximum principal stress varying  $w_t$  and  $t_b - t_s$  in (a) Model A and (b) Model B.

at the end of termination as  $t_b - t_s$  is smaller and  $w_t$  is greater. The greatest  $\sigma_{p, \max}$  is minimized when  $w_t = 626$ ,  $t_b - t_s = 50\text{--}100 \mu\text{m}$  in Model B. Within the given ranges of  $w_t$  and  $t_b - t_s$ , the effect of optimizing  $w_t$  and  $t_b - t_s$  on reducing peak stress seems to be greater in Model B than in Model A. The effects of  $w_t$  and  $t_b - t_s$  on the greatest  $\sigma_{p, \max}$  in Models A and B are also summarized in analytical formulation by regression as follows:

$$\sigma_{p, \max}^{\text{Model A}} = 106.2 + 14.1w_t^o + 10.4t_b^o + 19.8w_t^{o2} - 1.6w_t^o t_b^o + 5.4t_b^{o2} \quad (1)$$

$$\sigma_{p, \max}^{\text{Model B}} = 123.1 - 22.2w_t^o - 18.4t_b^o + 21.7w_t^{o2} - 17.5w_t^o t_b^o - 3.8t_b^{o2}, \quad (2)$$

where  $\sigma_{p, \max}^{\text{Model A}}$  and  $\sigma_{p, \max}^{\text{Model B}}$  are the greatest  $\sigma_{p, \max}$  in Models A and B, respectively. The  $w_t^o$  and  $t_b^o$  are mapped values in which the actual highest and lowest values of  $w_t$  and  $t_b$  are made to be 1 and  $-1$ , respectively. The maximum and minimum values of each model are in given Table III. In Eqs. (1) and (2), the electrode thickness is represented by the bottom thickness  $t_b$ , and the corresponding  $t_s$  to minimum, medium, and maximum  $t_b$  are described in Figs. 7(a) and (b).

## (2) Experimental Result

Board flex test specimens were prepared following the procedure described in Section II(3). The test results are shown in Fig. 8 with MLCC model configurations. Unfortunately,  $w_t$  and  $t_b - t_s$  could not be controlled separately in the production process.  $t_b - t_s$  tends to increase with  $w_t$ . Hence, in the four types of MLCC samples in Fig. 9,  $t_b - t_s$  is larger as chip thickness and  $w_t$  are greater. With smaller  $w_t$ , all the samples of Models A and B

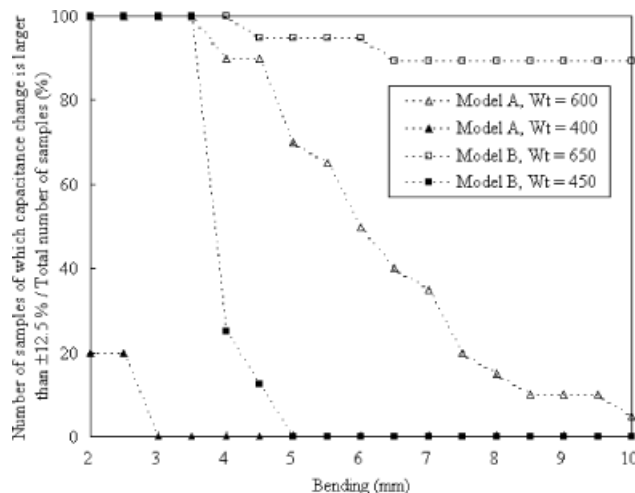


**Fig. 8.** Ratio of the number of samples where capacitance change is larger than  $\pm 12.5\%$  to the total number of samples versus the degree of bending.

are fractured under 3 and 5 mm bending, respectively. Increasing  $w_t$  by 200  $\mu\text{m}$ , in 90% of samples of Model B, capacitance change does not occur until 10 mm bending. For the same increase of  $w_t$ , the resistance to cracking of the samples of Model A had also improved; however, the improvement was substantially lower than in Model B. This finding agrees with the calculation result that a similar level of increase of  $w_t$  decreases the greatest  $\sigma_{p,\max}$  to a larger degree in Model B than in Model A.

Figures 9(a) and (b) show SEM images of cross sections of fractured samples. Fig. 9(a) shows the typical crack shape and path observed in the cross section of fractured samples of Models A and B. As shown in Fig. 9(a), most of the cracks in Models A and B seem to be initiated at the end of termination and the crack path is angled away from the MLCC center. The crack

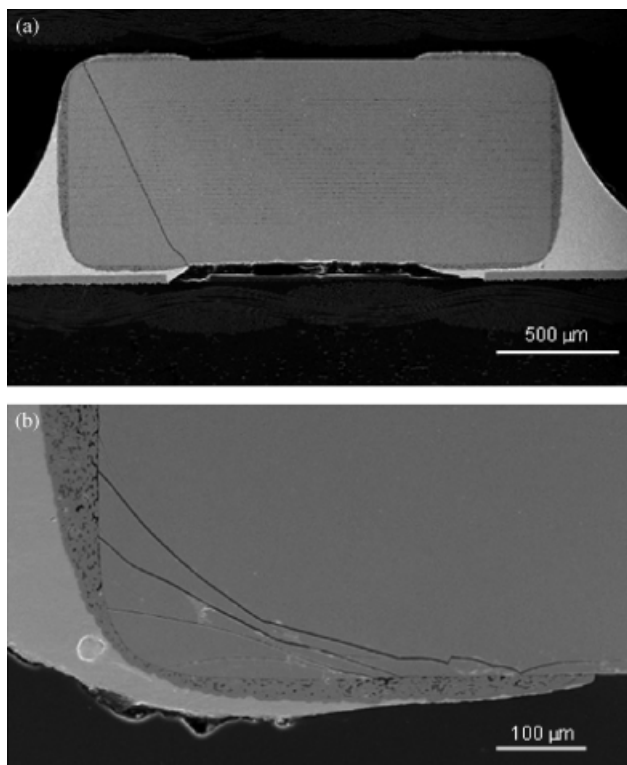


**Fig. 9.** Scanning electron microscopy (SEM) images of (a) Model A with a crack and (b) Model B with multiple cracks induced on the interface.

ends in the upper interface between the termination and the ceramic in Model A and, in Model B, it stops at the side interface. In Model B, crack initiation at the bottom interface is also observed in the specimens with larger  $w_t$  as in Fig. 9(b). In this case, multiple crack initiation is observed and the crack propagation ends in the side interface close to the bottom. The interface crack could not be detected by capacitance change as it does not propagate across the active layers. This crack was detected by acoustic emission and inspection of external surfaces under an optical microscope.

Using an appropriate polishing procedure, the surface was observed under OM and the crack path was traced. In the MLCC where the crack is initiated at the end of termination, a three-dimensional crack path is schematically described in Fig. 10. The red lines indicate where the fracture surface meets the external surfaces of MLCCs, and the blue lines indicate where the fracture surface meets three central cross sections. Figure 10 shows that crack propagation on the bottom surface is along the termination edges. In Model A, the end of cracks (C in Fig. 10) is on the top interface and is on the side interface in Model B.

#### IV. Discussion

In Section III(1), the stress induced in the MLCC in the board flex test is calculated for 3 mm bending. It has been assumed that (1) the magnitude of stress will be increased with the degree of bending; however, (2) the effect of design parameters on the stress will remain similar as in Eqs. (1) and (2) and in Fig. 7 regardless of the degree of bending. The experimental results in Fig. 8 showed good agreement with the calculation results in Fig. 7 and the assumptions that increasing  $w_t$  improved the resistance to cracking significantly in both Models A and B. Under more than 5 mm bending, the bending strength of Model B had improved to a greater degree than Model A, which also corresponds to the simulation results in Fig. 7. However, under  $<4.5$  mm bending, Model B with small  $w_t$  showed a much higher survival probability than Model A with similar  $w_t$ , which is difficult to explain based only on the simulation results in Fig. 7. In addition, in the test results of Model A, the effect of increasing  $w_t$  on improving bending strength was obvious throughout the bending ranges, but it was not in Model B under  $<4$  mm bending. This fact conflicts with our assumptions. The bending strength of the ceramic is also affected significantly by defects such as pores and microcracks<sup>9</sup> because the defects are important factors determining the intrinsic crack resistance of the ceramic. Hence, microstructural analysis is necessary before the board flex test.

Based on the FEM results (Eqs. (1) and (2)),  $t_b - t_s$  is the second most important parameter for the stress. However, the effect of varying  $t_b - t_s$  on the bending strength could not be verified experimentally.  $t_b - t_s$  increases with  $w_t$  under the current production process, which may have contributed to the greater improvement in the bending strength of Model B than A (Fig. 8) according to the calculation results in Fig. 7. In addition, the fact that the greatest  $\sigma_{p,\max}$  occurs on the interface in Models B with large  $w_t$  also seemed to contribute to the better strength improvement in Model B. The interface is stronger inherently for a crack to be initiated under the same stress.<sup>17</sup> Although interfacial stress is much higher than the peak stress at the end of termination in Model B with large  $w_t$ , this does not necessarily mean that interfacial cracking occurs before crack initiation at the termination end. Also, there are fewer chances of forming defects such as microcracks, where cracks are initiated, on the interfaces than the ceramic adjacent to the termination ends because the interfaces are protected during manufacturing processes.

Simulation results showed the important effect of  $T_C/T_B$  on the stress and dependency of stress on design parameters. Until the soldering processes, the effects of  $w_t$  and  $t_b - t_s$  on the greatest  $\sigma_{p,\max}$  and stress distribution in MLCC showed the same ten-



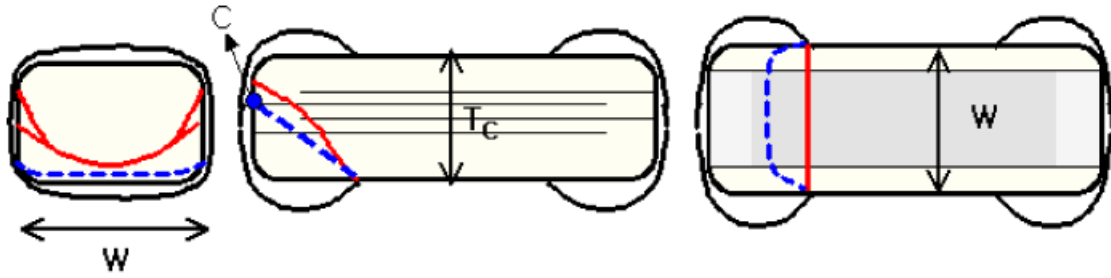


Fig. 10. Schematic description of the three-dimensional crack path.

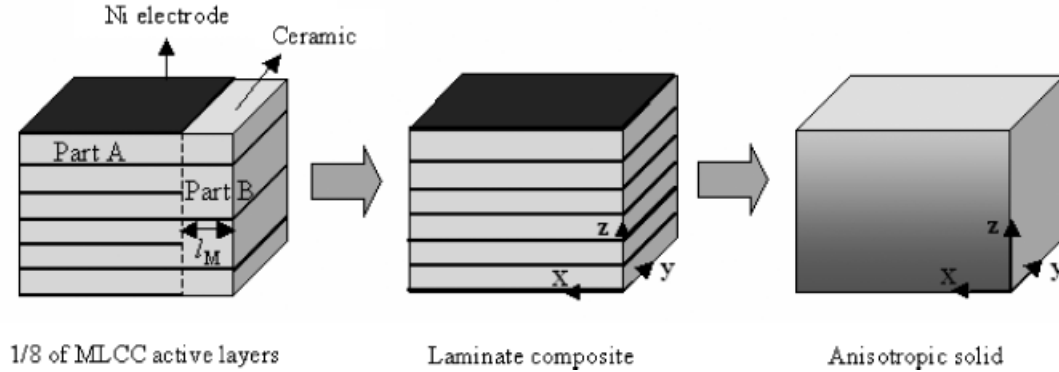


Fig. A-1. Composite models of MLCC.

dependency in Models A and B. In Model A ( $T_C/T_B \approx 0.5$ ), the bending load increases the greatest  $\sigma_{p,max}$  in MLCC, but does not change the functional dependency on  $w_t$  and  $t_b - t_s$ . However, in Model B, which has higher  $T_C/T_B$  ( $\approx 0.8$ ) than Model A, the stress increase by bending load concentrates on the bottom interfaces with the termination; hence, the dependency of the stress on  $w_t$  and  $t_b - t_s$  is enhanced. According to the calculation results in Fig. 7, if  $T_C/T_B$  as well as  $w_t$  and  $t_b - t_s$  can be modified by increasing the cover size, more stress can be reduced in Model A. However, the sizes of the design parameters such as the cover, the margin, and the termination are usually limited to certain values as required in major applications.

According to the two-dimensional FEM results of Franken *et al.*,<sup>3</sup> solder shape is one of the most important parameters affecting  $\sigma_{p,max}$ . This contradicts our simulation results that soldering does not change the stress state induced in termination firing considerably, which has been verified in our previous experiments.<sup>18</sup> On cooling from termination firing temperature, thermal residual tensile stress is also induced adjacent to the active layers as mentioned in Section III(1). The stress can cause cracking inside MLCC, mostly at the end of Ni electrodes below two covers.<sup>6</sup> Although this cracking has not been observed in the MLCC models analyzed in this study, the high tensile stress inside the MLCC has been an important issue particularly in high-capacitance MLCC with a large number of active layers.<sup>19</sup>

## V. Conclusions

Using three-dimensional FEM simulation, the design parameters that played the greater role in reducing thermo-mechanical stress induced in the MLCC have been investigated. According to the FEM results, the width ( $w_t$ ) and thickness ( $t_b - t_s$ ) of the Cu termination have been found to be the most dominant parameters affecting the stress. It is also affected by the thickness ratio of the MLCC to the board ( $T_C/T_B$ ). The simulation results have been verified by the board flex test of the samples with different  $T_C/T_B$  and  $w_t$ . The samples with a larger  $w_t$  were fractured at a higher degree of bending and the beneficial effect of increasing  $w_t$  in improving bending strength was greater in the samples of larger  $T_C/T_B$ . The crack initiation occurred at the end of termination in most samples, but multiple crack initiation on

the interface has been observed in the samples with large  $w_t$  and  $T_C/T_B$ . The experimental results agree well with the predictions based on the FEM calculations using the greatest  $\sigma_{p,max}$  as a metric.

## Appendix A: Effective Material Properties of Anisotropic Solid

### (A.1) CTE ( $\alpha$ )

$$\alpha_X = \alpha_Y = \frac{f_d \frac{E_d}{1-\nu_d} \alpha_d + f_e \frac{E_e}{1-\nu_e} \alpha_e}{f_d \frac{E_d}{1-\nu_d} + f_e \frac{E_e}{1-\nu_e}}$$

$$\alpha_Z = (f_d \alpha_d + f_e \alpha_e) - \left( f_d \frac{2\nu_d}{1-\nu_d} + f_e \frac{2\nu_e}{1-\nu_e} \right) \alpha_X$$

$$+ \left( f_d \frac{2\nu_d}{1-\nu_d} \alpha_d + f_e \frac{2\nu_e}{1-\nu_e} \alpha_e \right)$$

where  $\nu$  is Poisson's ratio and  $f$  is volumetric ratio (subscripts d, e: dielectric ceramic layer, electrode, respectively).

### (A.2) Young's Modulus ( $E$ )

$$E_X = E_Y = f_d E_d + f_e E_e$$

$$E_Z = \frac{E_d E_e}{f_d E_e + f_e E_d}$$

where  $\nu$  is Poisson's ratio and  $f$  is volumetric ratio (subscripts d, e: dielectric ceramic layer, electrode, respectively).

## References

- H. Kishi, Y. Mizuno, and H. Chazono, "Base-Metal Electrode-Multilayer Ceramic Capacitors: Past, Present, and Future Perspectives," *Jap. J. Appl. Phys.*, **42**, 1-15 (2003).
- G. C. Scott and G. Astfalk, "Thermal Stresses in Multilayer Ceramic Capacitors: Numerical Simulations," *IEEE Trans. Components, Hybrids, Manuf. Tech.*, **13**, 1135-45 (1990).
- K. Franken, H. R. Maier, K. Prume, and R. Waser, "Finite-Element Analysis of Ceramic Multilayer Capacitors: Failure Probability Caused by Wave Soldering and Bending Loads," *J. Am. Ceram. Soc.*, **83**, 1433-40 (2000).

<sup>4</sup>M. J. Cozzolino and G. J. Ewell, "A Fracture Mechanics Approach to Structural Reliability of Ceramic Capacitors," *IEEE Trans. Components, Hybrids, Manuf. Tech.*, **CHMT-3**, 250–7 (1980).

<sup>5</sup>*Multilayer Ceramic Capacitors—General*. Samsung Electro-Mechanics, Suwon, Korea, pp. 1–35. (<http://www.sem.co.kr/en/indexMain.jsp>).

<sup>6</sup>J. Maxwell, *Technical Information—Cracks, the Hidden Defects*. AVX Corporation, South Carolina, USA. (<https://www.avx.com/docs/techinfo/cracks.pdf>).

<sup>7</sup>K. Prume, R. Waser, K. Franken, and H. R. Maser, "Finite-Element Analysis of Ceramic Multilayer Capacitors: Modeling and Electrical Impedance Spectroscopy for a Nondestructive Failure Test," *J. Am. Ceram. Soc.*, **83**, 1153–9 (2000).

<sup>8</sup>K. Prume and K. Franken, "Modeling and Numerical Simulation of Electrical, Mechanical, and Thermal Coupled Behavior of Multilayer Capacitors," *J. Eur. Ceram. Soc.*, **22**, 1285–96 (2002).

<sup>9</sup>J.-W. Park, P. F. Mendez, and T. W. Eagar, "Strain Energy Distribution in the Ceramic-to-Metal Joints," *Acta Mater.*, **50**, 883–99 (2002).

<sup>10</sup>S. Timoshenko, *Strength of Materials*, p. 88. Krieger, Huntington, NY, USA, 1976.

<sup>11</sup>C. T. Sun and S. Li, "Three-Dimensional Effective Elastic Constants for Thick Laminates," *J. Comp. Mater.*, **22**, 629–39 (1988).

<sup>12</sup>C. T. Sun and W. C. Liao, "Analysis of Thick Section Composite Laminates Using Effective Moduli," *J. Comp. Mater.*, **24**, 977–93 (1990).

<sup>13</sup>ASM International. *Metals Handbook*, 2nd edition, ASM International, Materials Park, OH, 1998.

<sup>14</sup>R. C. Dunne and S. K. Sitaraman, "The Effect of Substrate Materials on the Thermo-Mechanical Behavior of Multilayered Structures"; pp. 134–8 in *Proceedings of International Symposium on Advanced Packaging Materials*. IEEE, Braselton, GA, USA, 1997.

<sup>15</sup>ABAQUS ver. 6.4-1, HKS, 2003.

<sup>16</sup>DOE PRO XL, Air Academy Associates and LLC Digital Computations.

<sup>17</sup>A. G. Evans, B. J. Dalgleish, M. He, and J. W. Hutchinson, "On Crack Path Selections and the Interface Fracture Energy in Bimaterial Systems," *Acta Metall.*, **37**, 3249–54 (1989).

<sup>18</sup>J.-W. Park, I. H. Park, and H. J. Yoon, submission in progress.

<sup>19</sup>Y. I. Shin, K. M. Kang, Y. G. Jung, J. G. Yeo, S. G. Lee, and U. Paik, "Internal Stresses in BaTiO<sub>3</sub>/Ni MLCC," *J. Eur. Ceram. Soc.*, **23**, 1427–34 (2003). □